communications physics

Article

https://doi.org/10.1038/s42005-024-01869-2

Exploring the potential of self-pulsing optical microresonators for spiking neural networks and sensing

Stefano Biasi [1,2] ✉, Alessio Lugnan [1,2], Davide Micheli[1] & Lorenzo Pavesi [1]

Photonic platforms are promising for implementing neuromorphic hardware due to their high processing speed, low power consumption, and ability to perform parallel processing. A ubiquitous device in integrated photonics, which has been extensively employed for the realization of optical neuromorphic hardware, is the microresonator. The ability of CMOS-compatible silicon microring resonators to store energy enhances the nonlinear interaction between light and matter, enabling energy efficient nonlinearity, fading memory and the generation of spikes via self-pulsing. In the self-pulsing regime, a constant input signal can be transformed into a time-dependent signal based on pulse sequences. Previous research has shown that self-pulsing enables the microresonator to function as an energy-efficient artificial spiking neuron. Here, we extend the experimental study of single and coupled microresonators in the self-pulsing regime to confirm their potential as building blocks for scalable photonic spiking neural networks. Furthermore, we demonstrate their potential for introducing all-optical long-term memory and event detection capabilities into integrated photonic neural networks. In particular, we show all-optical long-term memory up to at least 10 μs and detection of input spike rates, which is encoded into different stable self-pulsing dynamics.

Photonics provides unmatched benefits to neuromorphic computing, including high throughput, low latency, and energy efficiency of linear operations[1–3]. Still, achieving cascadable and energy efficient nonlinear operations, which are essential for artificial neural networks (ANNs), is notoriously challenging in photonics due to the absence of direct photon-photon interaction. Linear operations can be performed by photonic hardware to accelerate connections between layers of neurons, which can especially benefit large ANNs models hosted in data centers. On the other hand, edge computing applications often require smaller and more specialized ANNs to run on compact and cost effective hardware, which can learn continuously or can be easily re-trained to adapt to new working conditions[4,5]. Therefore, in many cases, photonic neuromorphic hardware for edge computing should comprise full ANNs, thus including energy-efficient nonlinear nodes. In particular, spiking neural networks (SNNs), where neurons produce and process time-dependent signals based on pulse sequences as in biological brains, are especially promising to achieve better trade-offs between computational power and efficiency[6,7]. In this work, we experimentally demonstrate practically useful properties (long-term memory and spike rate detection) of efficient and compact photonic spiking neurons (integrated microresonators) coupled together so as to form small networks.

Microring resonators (MRRs) are an ideal platform to induce light-matter interactions and thus enhance nonlinear phenomena. Nonlinear effects are typically caused by two-photon absorption (TPA) and the resulting free carrier absorption and dispersion (FCA and FCD)[8,9]. TPA generates free carriers in the conduction and valence bands, and the absorption of light and thermalization of free carriers induce heat in the waveguides. This leads to an increase in the silicon temperature and consequently a change in the refractive index related to the thermo-optic effect. The FCD and the thermo-optic effect induce a contrasting shift in the resonance frequency of MRR. Because of the effective refractive index dependence of the MRR resonance, the former shifts the resonance frequency toward the blue due to an increase in free carries concentration, while the latter shifts it toward red due to heating[10,11]. In addition to a contrasting shift, the two phenomena are characterized by two different relaxation times and a distinct optical field amplitude dependence. Indeed, the thermal and carrier lifetimes are typically of the order of (60–280) ns and (1–45) ns, respectively[12,13]. Moreover, the carrier concentration variation is governed by the square of field intensity, while the temperature variation is directly proportional to the field intensity[11]. Due to these different behaviours, the combination of thermo-optic, TPA, and FCD effects can induce

[1]Nanoscience Laboratory, Department of Physics, University of Trento, Trento, Italy. [2]These authors contributed equally: Stefano Biasi, Alessio Lugnan.
✉e-mail: stefano.biasi@unitn.it

self-pulsing (SP) oscillations. Here, a simple continuous wave input signal with a wavelength close to the resonance wavelength of the MRR is converted into an oscillating output signal caused by the nonlinear and oscillating resonance frequency shift[14,15]. This behaviour is named SP. By coupling few silicon MRRs in a series, a large variety of dynamic SP responses, including chaotic ones, can be obtained by varying the power and the wavelength of the input laser light[16].

Based on these effects, previous work has shown that silicon MRRs can be used as energy efficient artificial spiking neurons with low chip footprint[17–21], while others demonstrated the use of MRRs for neuromorphic computing[22]. In recent experiments, we have shown that several MRRs can be directly connected together to form relatively large and scalable neural networks on a photonic chip[23,24]. However, previous work involving artificial spiking neurons created by passive microresonators has primarily focused on emulating the basic functional properties enabled by SP. To the best of our knowledge, experimental studies about the use of SP MRRs at the system and at the application levels are still lacking.

In this work, we advance this research path by experimentally demonstrating relevant properties of the SP dynamics in systems comprising multiple coupled silicon MRRs, called Side-Coupled Integrated Spaced Sequences Of Resonators (SCISSORs). In particular, in comparison to previous works[17–21], we provide the following main original contributions:

- Exploration of the spiking frequencies and waveform shapes produced by SP in SCISSORs composed of 2 and 3 MRRs, which are compared to the single MRR case. A relevant finding is that the maximum spiking frequency increases notably along with the number of coupled MRRs (see "Self-pulsing dynamics" section).
- Demonstration of all-optical long-term memory (at least 10 μs) enabled by SP regimes, lasting much longer than the memory intrinsic to the silicon nonlinear effects (see "Long-term memory enabled by self-pulsing" section).
- Evidence that the SP dynamics of a SCISSOR are sensitive to perturbations of the optical input consisting of spike sequences with certain spike rates. Specifically, there exist special SP regimes where the system dynamics are permanently and selectively modified depending on the spike rate of the perturbation, thus enabling all-optical spike rate detection (see "Spike rate detection" section).

It should stressed that, the fact that a simple 2-ring or 3-ring SCISSOR can be activated by certain spike rates and can also generate different spike rates (and spike shapes), corroborates their potential as building blocks for complex and scalable all-optical SNNs. Moreover, by demonstrating that SP in a SCISSOR can greatly extend the memory duration of the device and can map different input pulse rates into different average output powers, we highlight its potential for high-speed and energy efficient optical sensing and computing. Therefore, we believe that this work provides important elements to bridge the existing component-level studies to future system-level developments and applications, regarding the use of silicon MRRs as nonlinear dynamic units for neuromorphic computing.

Results

The devices under test include a MRR in an add-drop configuration as well as two SCISSOR structures, one consisting of two coupled MRRs and the other consisting of three coupled MRRs (see "Samples" subsection in the Methods for more details and a sketch of the device geometries). Their optical response was measured using a standard setup that included a fiber-coupled tunable CW laser, an erbium-doped fiber amplifier (EDFA), an electro-optic modulator, and a fiber array to couple the light signal to the devices (see "Experimental setup" in the Methods for details). These were excited with different amplitude-modulated input signals, scanning different frequencies and powers of the input laser. Each response was examined using mathematical-statistical methods to identify similarities, distinct patterns, and net changes resulting from variations in specific properties of the input signal.

In the following, we divide the results and their analysis into three subsections. In the first, we analyse the dynamics of the SP regime. In the second, we see how SP can impart long-term memory. In the last one, we show the ability of a SCISSOR to discriminate different spike rates over a carrier-modulated signal. Among the various results, we have selected some instructive cases, which reveal the potential of the analyzed structures as SNN building blocks and for sensing applications.

Self-pulsing dynamics

In this section we demonstrate different SP dynamics that depend on the power and frequency of the input laser. Such a diversity in response lies not only in the spike rates, but also in the different temporal line shapes that can be generated. For each structure, we report the optical response measured at the drop port. Specifically, we present the results with various figures where we show the spectral shape in the linear regime (low power) and a color map (called SP map) indicating the lowest frequency of the SP oscillation as a function of the mean input optical power and frequency of the input laser. The displayed SP frequency is the one associated with the pattern that repeats periodically with the longest period in the time response. The SP map is flanked by four graphs showing a window of the SP temporal lineshape associated with a specific laser frequency and power points. These are indicated on the map by a spiral, a star, a square or a circle. In particular, the black line shows the time response, while the red dashed line is a sine curve that matches the fundamental SP frequency, which is the one reported in the SP map.

Figure 1 shows our results for the single MRR. The spectral response in the linear regime (Fig. 1(a)) presents the typical Lorentzian shape, where the quality factor is about $Q \simeq 1.092 \times 10^4$. The SP map (Fig. 1(b)) shows that by increasing the laser power while approaching the cold MRR resonance frequency from low frequencies, the MRR enters in a SP regime. This is observed in the map by a change in the color from the blue to the red. The SP map shows a series of oscillation states (non-zero frequency points). We observe that the SP frequency decreases as the laser frequency increases. The time trace in Fig. 1(b1), indicated by the spiral corresponds to a low-power point away from the cold resonant frequency of the MRR (where transmission is linear). It shows the 80 μs period square wave used as input excitation signal. The square wave is deformed by the non-ideal AWG response. It should be stressed that this does not limit our study of SP dynamics but enriches the measured response by highlighting the sensitivity of the different devices to the input signals. In fact, we verified that the observed SP frequencies coincides with those obtained using a continuous wave excitation despite the different turn-on and turn-off ratios. Here, we report the measurements with a square wave excitation because it allows a comparison between different *on* plateaus, allowing us to verify reproducibility in the SP frequency measurements. This is facilitated by the *off* plateau, which resets the initial state of the MRR, ensuring that the response is consistent at the beginning of each *on* plateau. A typical MRR exhibits complex behavior, ranging from the characteristic SP pattern (graph marked with a star, Fig. 1(b2))[13], to an irregular pattern with varying spacing between peaks (graph marked with a square, Fig. 1(b3)), to a fast sinusoidal-like oscillation (graph marked with a circle, Fig. 1(b4)). The SP frequency varies quasi-continuously on the left shoulder of the Lorentzian, while showing scattered, i.e., more discontinuous regions, near the resonance frequency. Indeed, for most states, the MRR reaches a stable oscillation in the first 10 μs of the on-state plateau, which persists until the off-state. Only the discontinuous SP region shows temporal optical responses with a variable oscillation period in the 40 μs window, as shown in the trace marked by the square (Fig. 1(b3)).

The sinusoidal-like oscillation (graph marked with a circle in Fig. 1(b4)) shows the maximum SP frequency of (7.25 ± 0.02) MHz. This SP state occurs at relatively low average input power and does not show the typical SP pattern (graph marked with a star, Fig. 1(b2)). To verify the existence of these SP regimes, we simulated the response of a MRR using the Matlab-based library Photonic hybRid EleCtromagnetic SolvEr (PRECISE)[25]. In the simulations, the linear characteristic parameters, such as the intrinsic and extrinsic coefficients, were estimated from a fit of the linear response shown in Fig. 1(a), while the nonlinear parameters were obtained from[13]. Thus, we simulated the time evolution of the complex field

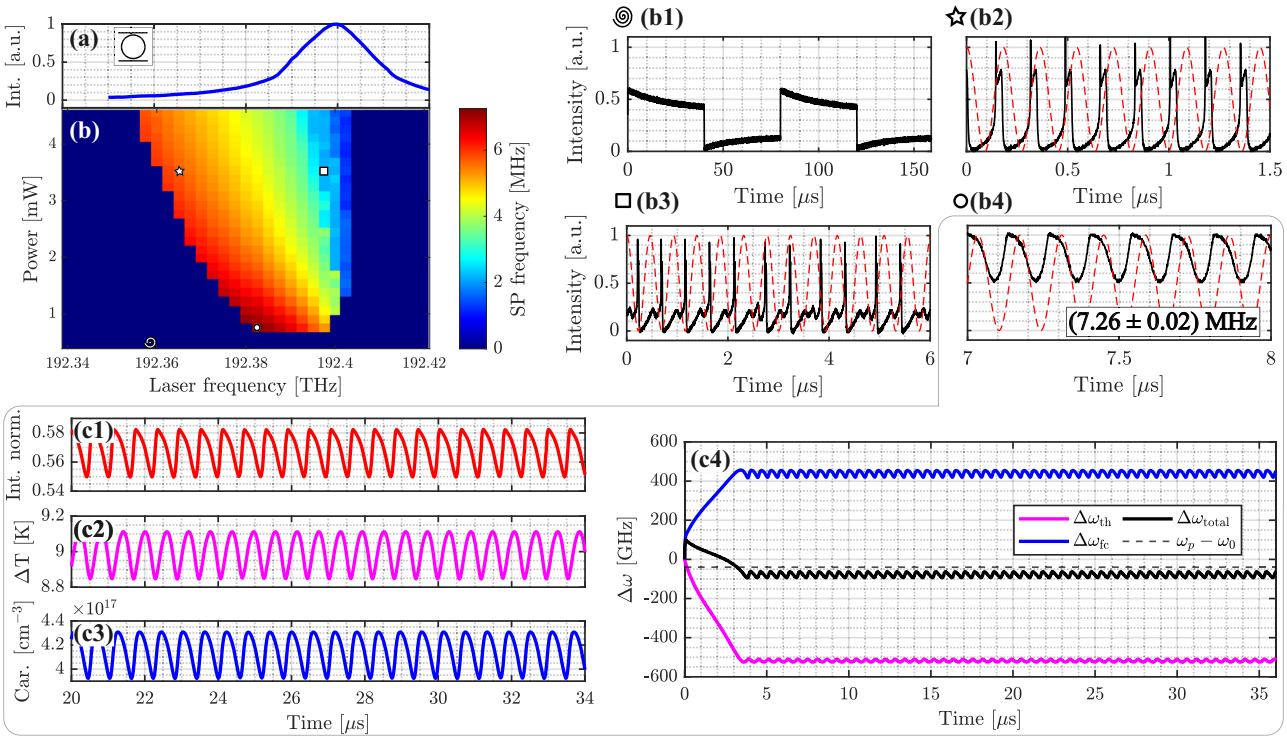

Fig. 1 | SP regimes of the single MRR. a The experimental spectrum depicts the drop port transmission in the linear regime. This corresponds to the cold resonance spectrum. **b** The colored map shows the SP map. Here the SP oscillation frequency are mapped as a function of the input laser frequency and the average input optical power. Frequencies are color coded according to the color bar on the right. The reference constant (linear) region is coded with a dark blue color. On the right there are four graphs **(b1)**–**(b4)** which refer to the different symbols (points) in the SP map. The SP temporal drop intensity lineshapes are here reported for different excitation conditions corresponding to the symbols (spiral (b1), star (b2), square (b3), circle (b4)) on the SP map. The black solid and red dashed curves represent the optical response and a sine curve corresponding to the fundamental SP frequency, respectively. The graphs within the box, particularly panels (b4) and **(c1)**–**(c4)**, highlight a peculiar SP regime where the drop intensity oscillates with a sinusoidal lineshape. (c1)–(c4) report the simulations that replicate the sinusoidal-like oscillation. Specifically, the time traces show the drop intensity output ((c1), red line), the MRR temperature change ((c2), magenta line), and the free carrier concentration change ((c3), blue line). **(c4)** shows the resonance frequencies shift versus time due to the different nonlinear effects (magenta contribution to the shift due to the temperature, blue due to the free carrier concentration, black total frequency shift, dashed line input laser frequency). The frequencies are all referrred to the cold resonance frequency ω_0.

in the MRR, together with TPA, FCA, FCD, and thermo-optical dispersion. The obtained results are shown in the yellow box in Fig. 1(c1)–(c4). Here we show, as a function of time, the output drop intensity of the MRR ((c1) with the red line), the temperature difference between the MRR and its surroundings ((c2) with the magenta line) and the free carrier concentration ((c3) with the blue line). All these quantities oscillate periodically in time due to the SP regime, which is ruled by the interplay between the FCD and thermo-optic effects. These in turn have a different dependence on the optical field intensity. It should be noticed that the sinusoidal behavior is characterized by a peculiar dependence on the laser frequency. Indeed, the sinusoidal lineshapes form only when the laser frequency is higher than the cold MRR resonance frequency and the induced frequency shift does not overpass the input laser frequency. This is demonstrated by the simulation reported in the Fig. 1(c4). Here, the change in the resonance shift due to the contribution of the thermal effect ($\Delta\omega_{th}$), the free carrier concentration ($\Delta\omega_{fc}$), the sum of the two ($\Delta\omega_{total}$), and the difference between the input laser frequency and the resonant frequency (ω_p–ω_0) are shown with the magenta, blue, black solid lines and the black dashed lines, respectively. Sinusoidal-like oscillations are characterized by the fact that $\Delta\omega_{total}$ never exceeds the reference of the input laser (ω_p–ω_0), in contrast to the typical SP regime[11].

Figure 2 shows our results for the 2-ring SCISSOR (panels (a)–(b4)) and the 3-ring SCISSOR (panels (c)–(d4)). In both cases, the cold resonances of the MRRs exhibit overlapping features, resulting in a quasi-plateau in the linear regime spectrum (see graphs (a) and (c)). The two SCISSORs exhibit SP maps (panels (b) and (d)) characterized by multiple SP regimes and richer dynamics than the simple MRR. Both exhibit modes with a maximum SP frequency at low average input powers. These SP oscillations are shown in the time traces indicated by the circle (panels (b1)) and (d1)). They resemble the sinusoidal-like oscillation of the single MRR, but with a more complex pattern and a high oscillation frequencies of about (12.3 ± 0.01) MHz and (21.24 ± 1.09) MHz for the 2-ring and 3-ring SCISSOR, respectively. The traces marked by the star (panels (b2) and (d2)) show SP modes with low spike rates that exhibit a periodic pattern consisting of a well-defined set of spikes. For the SCISSORs, especially the one with three rings, the SP oscillations evolve over time and typically reach a well-defined frequency only in the last 10 μs of the *on* plateau. Time traces marked with a square (panels (b3) and (d3)) show a change in the SP frequency over time, which for the 3-ring SCISSOR also results in the appearance of more spikes in the periodic pattern. Time traces of SP boundary modes are indicated by the spiral (panels (b4) and (d4)). For the 2-ring SCISSOR, the mode evolves from a low SP frequency to a non-oscillating state in 30 μs. Conversely, the 3-ring SCISSOR shows a dynamic evolution of the spike rate over about 40 μs, going from an SP oscillation of about 20 MHz to 1.8 MHz, accompanied by distinct patterns (see inset in Fig. 2(d4)).

Let us close this discussion with a note of cautious about the SP maps. These maps are useful to define the operating regimes of the SCISSORs. However, the map is specific to each actual SCISSOR, meaning that it is influenced by the used fabrication technology, by the nominal design parameters of the MRRs and by the fabrication uncertainties. As a result, different fabrication runs of the same design in the same foundry yield structures with slightly different SP maps due to fabrication fluctuations which cause uncontrolled variations in the nonlinear parameters (e.g., the free carrier lifetime or the thermo-optic coefficient). However, this does not prevent the

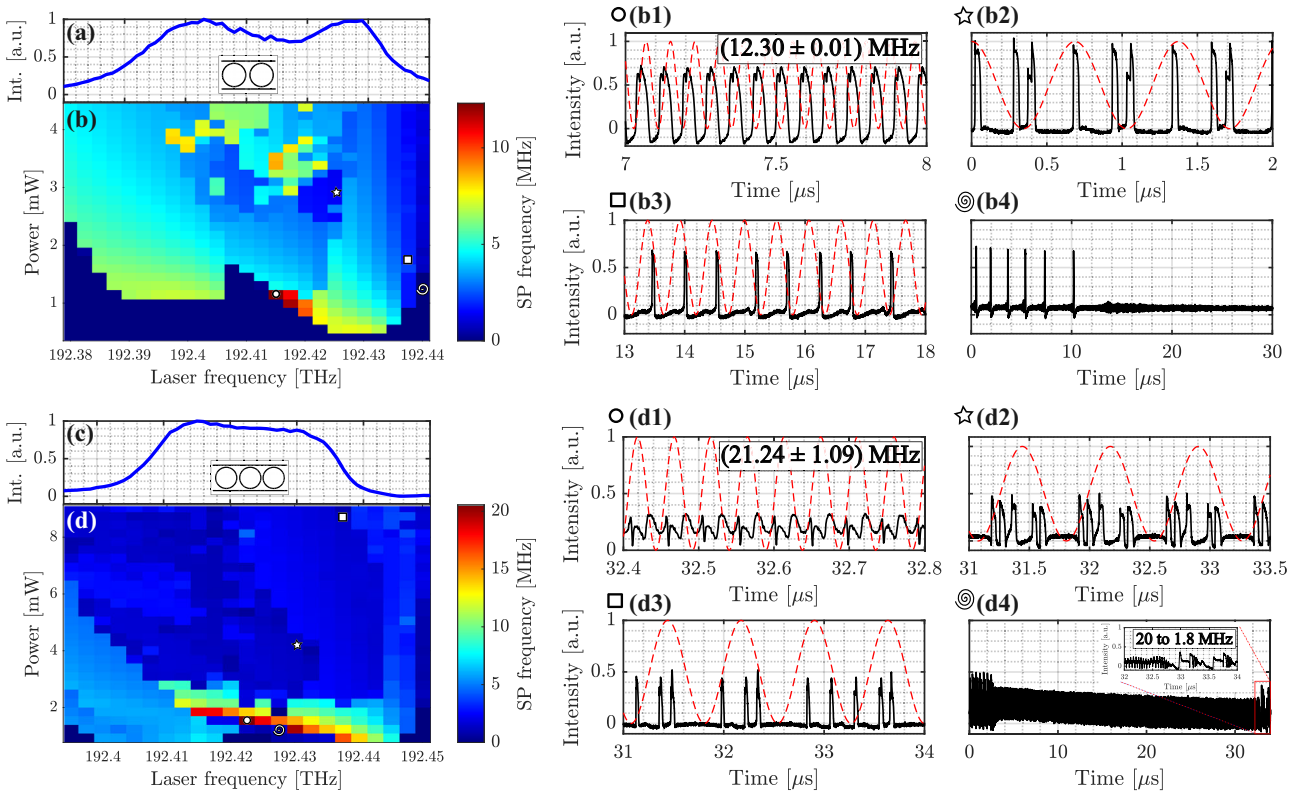

Fig. 2 | SP regimes of the 2-ring and 3-ring SCISSOR. Specifically, **(a)**–**(b4)** and **(c)**–**(d4)** correspond to the 2-ring and 3-ring SCISSOR, respectively. **(a)** and **(c)** report the experimental dropt intensity spectra in the linear regime. **b**, **d** Show the SP map as a function of the laser frequency and average input optical power. The side graphs (**b1**)–(**b4**) and (**d1**)–(**d4**) show the temporal responses associated with different points in the SP map identified by the different symbols (circle, star, square, and spiral). The black solid (red dashed curves) represents the optical response (a sine curve corresponding to the fundamental SP frequency). The inset in the graph (d4) shows the change in SP frequency by zooming in on the region highlighted by the red rectangle. Note that in the 2-ring (b) and 3-ring SCISSOR (d) SP maps, both the time and power scales are different.

use of coupled MRRs as neuromorphic hardware; it simply requires an initial characterization of the SP map to understand their working regimes.

Long-term memory enabled by self-pulsing

MRRs feature two different fading memory mechanisms due to relaxation of the free carrier density and to the variation of the temperature, whose characteristic times are (1–45) ns and (60–280) ns respectively. In previous works these effects were exploited for neuromorphic computing based on photonic reservoir computing[24,26]. In this section we show that the SP dynamics in silicon MRRs enable memory lasting much longer (ideally forever) than the aforementioned fading memory directly arising from silicon nonlinear effects. Such a long-term memory expands the applicability of MRRs -based neuromorphic computing to problems with a much broader range of timescales, as it can connect events separated by a relatively long time period. An example is given by fiber sensing applications, where timescales are usually much longer than a microsecond.

We demonstrate the long-term memory effect by first triggering and sustaining the SP regime, then by perturbing the system with an input optical pulse, and finally by checking the SP output after a relatively long time (maximum 10 μs). We do so by inserting into our SCISSORs a series of middle-power (half the maximum optical power) rectangular pulses lasting 10 μs, separated by low-power pauses of the same duration (see Fig. 3(a). The role of the middle-power pulses (from now on referred to as *SP stages*) is to sustain SP dynamics in the MRRs, while the low-power pauses allow us to reset the MRRs state between the SP stages, so as to make them reproducible. In addition, a short high-power pulse (60 ns, from now on refrered to as *perturbing pulse*) was used to perturb the SP stages. It should be noticed that, the time t_p of the perturbation pulse w.r.t. the beginning of the corresponding SP stage, is gradually increased as the SP stages follow one another. For example, in Fig. 3(a1), the perturbing pulse is at the beginning of the SP stage, gradually moving to later times in the following SP stage, until it reaches the end (Fig. 3(a2)). At the end of each SP stage, an additional high-power short pulse serves as a reference for data analysis, without affecting the results presented in this article. The complete series of SP stages shown in Fig. 3(a) is divided into a first half (50 SP stages), called *perturbed*, where the perturbation occurs during the SP stage. In the second group of 50 SP stages, called *unperturbed*, the perturbation lays outside the SP stage (Fig. 3(a3)), gradually approaching the beginning of the next (Fig. 3(a4)).

To detect the target memory effects, i.e., the dependence of the SP dynamics on the short-pulse perturbation timing, we considered 26 points of the output waveform (spanning around 83 ns), taken at the end of each SP stage (excluding the final high-power short pulse). From now on, we refer to this 26-point waveform as the *test signal*, and we refer to its start time w.r.t. the beginning of the corresponding SP stage as t_{test}. Moreover, we define $\Delta t_p := t_{test} - t_p$ as the time between the perturbing pulse and the test signal, for the first 50 perturbed SP stages (see Fig. 3(a1)–(a4)). Note that Δt_p decreases from around 10 μs to 0 in the first 50 perturbed SP stages. For the second group of 50 unperturbed SP stages, we define $\Delta t_u := t_s - t_p$, where t_s is the start time of the SP stage subsequent to the considered perturbing pulse. In our study, Δt_p and Δt_u represent the time intervals used to assess memory.

By visually inspecting the acquired waveforms, it becomes clear that there exist SP-enabled memory effects, which are originated by a phase shift of the self-pulsations due to the perturbing pulse, which depends on Δt_p. A visual example is provided in Fig. 3(b), where the thunderbolt symbol indicates the approximate timing of the perturbation pulse in the

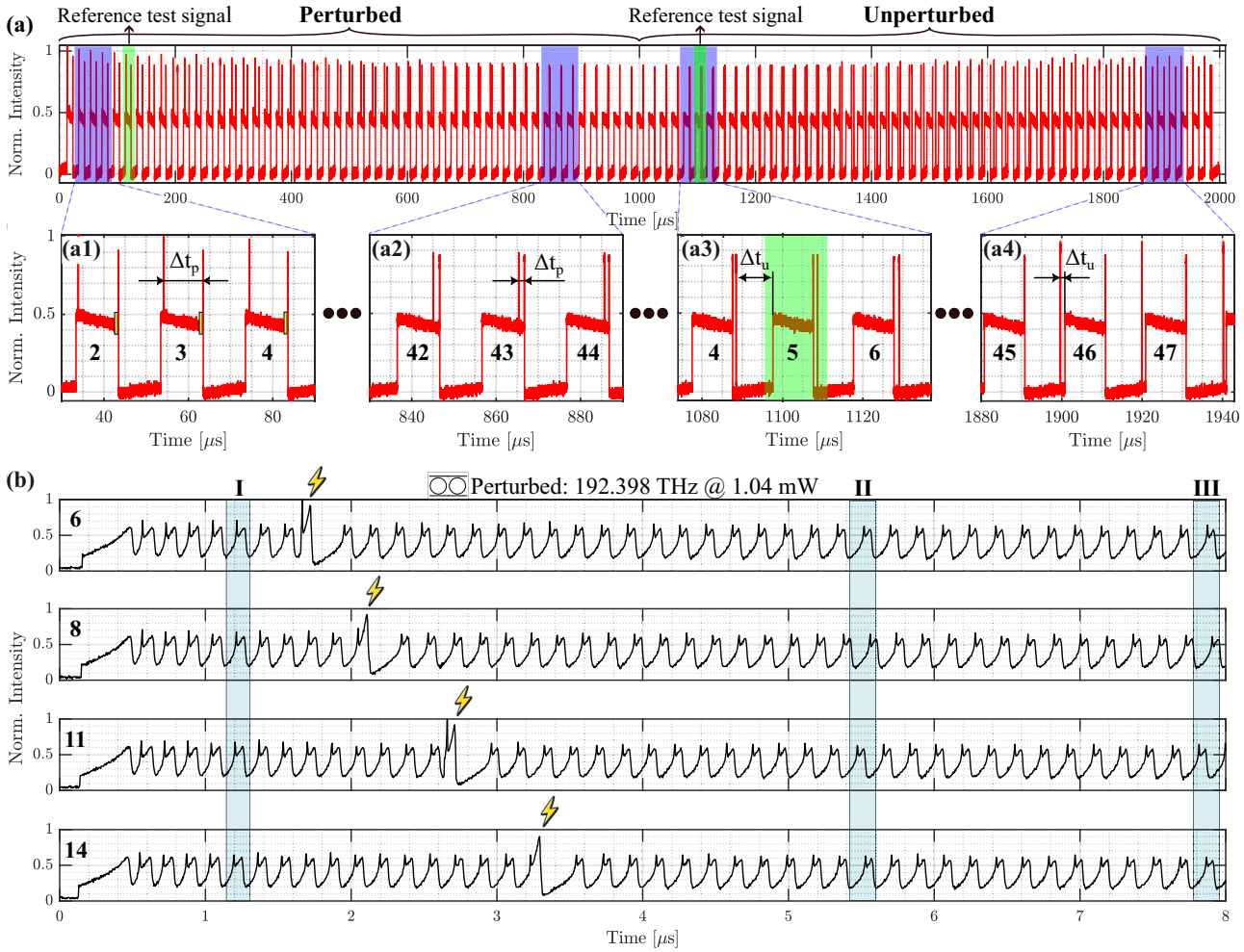

Fig. 3 | Long-term memory enabled by self-pulsing. a Input optical signal used to investigate memory effects, comprising 100 SP stages (that are the rectangular pulses used to sustain SP). The first 50 are called *perturbed* and the other 50 are called *unperturbed*, with the perturbing pulse inserted respectively during and before the SP stages. **(a1)–(a4)** Zoomed-in views showing the perturbing pulse gradually moving across ((a1) and (a2)) and past ((**a3**) and (**a4**)) the SP stage, corresponding to a gradual decrease of Δt_p and of Δt_u respectively for the perturbed and the unperturbed cases. The purple shaded areas in (**a**) highlight the zoomed part of (**a1**)–(**a4**). SP stage numbers are showed in bold format. The yellow rectangles at the end of the SP stages in (a1) indicate the position of the *test signal*. **b** Example output drop intensity waveforms corresponding to different SP stages (see numbers in bold format) showing the long-memory effect mechanism, that is, different SP phase shifts are induced by perturbation pulses at different timings (i.e., different Δt_p values), indicated by the Roman numerals. The thunderbolt symbols indicate the perturbing pulses timing. The blue shaded areas facilitate comparison between different SP stages in a given time window.

displayed waveforms. The blue rectangles labeled by Roman numerals (I, II, III) illustrate three different time periods across four distinct perturbed SP stages (6, 8, 11, 14). Prior to the perturbing pulse, the SP regime is in phase across these stages, as shown in rectangle I; the varying patterns are within the margin of experimental error alignment. However, following the perturbing pulse, all SP stages, except for stage 14 (lower waveform), become out of phase with respect to stage 6 (upper waveform), as highlighted by the rectangular II and III. It is noteworthy that stages 6 and 14, despite having different Δt_p values, display an in-phase SP regime even after the perturbing pulse. The periodic and reproducible SP states generated by rectangular pulses suggest that different perturbations merely cause a shift in the periodic pattern. As a result, for certain values of Δt_p, the SP states become aligned and in phase, as observed in traces 6 and 8. This effect depends not only on the power and frequency of the input but also on the characteristic parameters of the MRRs, especially their nonlinear properties. As this alignment is based on the phase relation between quasi-stable states, it can theoretically be maintained indefinitely, limited only by the duration of the SP states. This represents a long-term memory mechanism for the SCISSOR device. In the present work, the SP-enabled memory effects were monitored by measuring how much the test signal varies with the different Δt_p. This was done by calculating the correlation (Pearson correlation coefficient) between a reference test signal (taken from the sixth SP stage, see the green rectangle of Fig. 3(a)) and all the others. Looking at the obtained correlation estimations, we can distinguish between the following two main cases.

- If the correlation is high (close to one) it means that the test signal is not significantly perturbed w.r.t. the reference test signal. Therefore, no information about the perturbing pulse is conveyed to the subsequently measured test signal and thus no memory effect is detected for the considered Δt_p (or Δt_u for the unperturbed SP stages).
- If the correlation is low (significantly lower than one) it could be either because the measured test signals are noisy (purely noisy signals are uncorrelated) or because the presence of the perturbation signal significantly influences the subsequent test signal. Only in the latter case we detect an SP-enabled memory effect. These two cases can be distinguished by comparing the correlation value obtained in the *perturbed* case with the ones obtained in the corresponding *unperturbed* case. Indeed, in the case of noisy signals, correlation must be low for both the perturbed and the unperturbed cases. On the other hand, low correlation in the perturbed case and high correlation in the

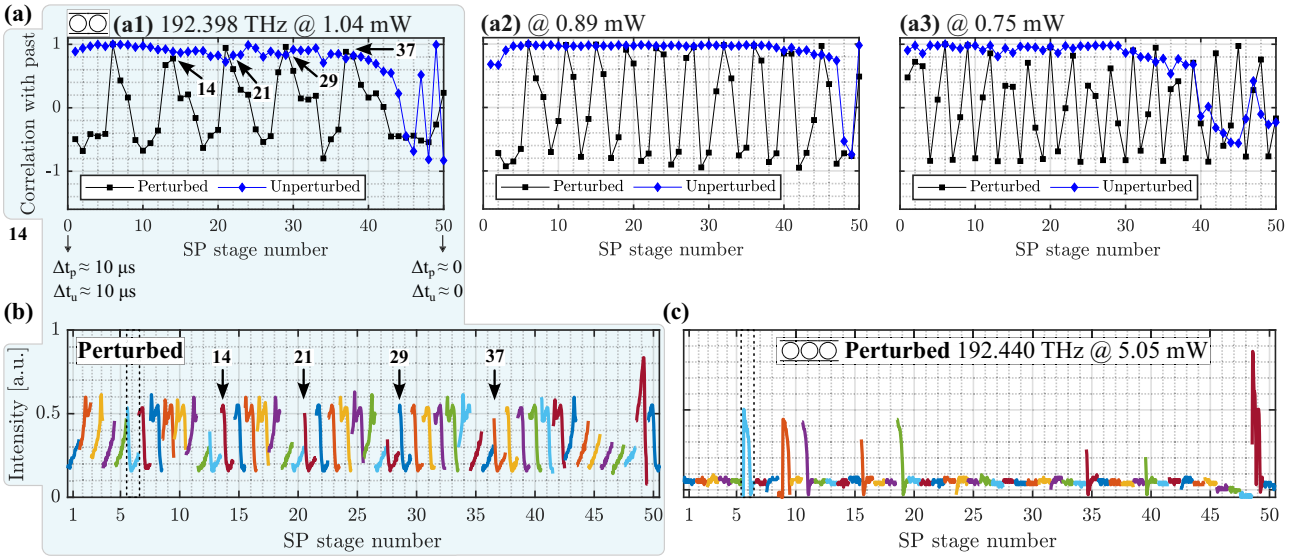

Fig. 4 | Detected memory effects. a correlation of the test signal with the reference test signal, as a function of the SP stage number in the two-ring SCISSOR. The three plots **(a1)**–**(a3)** correspond to different input power levels. The SP stage number is related to Δt_p (or to Δt_u for the unperturbed case). Here we compare memory effects when perturbations happen during a SP stage (perturbed case, black dots) and when they happen outside the SP stage (unperturbed case, blue dots), respectively. These two situations correspond with the first and second half of the plot in Fig. 3a. The bold numbers indicate the number of SP stages that show a correlation close to one. **b** Test signals from subsequent SP stage (represented by different colours), used to compute the correlation with past in plot (a1). The dotted vertical lines indicate the sixth SP stage used as the reference test signal in the correlation. **c** Test signals from a 3-ring SCISSOR, showing a non-periodic memory effect. In (b) and (c), since the time interval between successive sets of points is too long (20 μs), on the x-axis we report the SP stage number instead of the actual time, to make the visualization of the optical response clearer.

unperturbed case indicates an SP-enabled memory effect, since the difference between the perturbed and unperturbed cases is that, in the first case, the test signal is connected to the perturbing pulse by the SP dynamics.

We detected long-term memory effects (low correlation) oscillating periodically as the SP stage number increases, namely Δt_p decreases, for the *perturbed* SP stages (3 examples for the 2-ring SCISSOR are shown in Fig. 4(a), black data). As mentioned, we validated these results by comparing this analysis with its *unperturbed* counterpart (Fig. 4(a), blue data), i.e., the correlation of test signals from the *unperturbed* SP stages. Indeed, for the unperturbed case, we do not observe long-term memory effects, since the correlation is high except for small Δt_u values. The short-term memory in the unperturbed case (i.e., for small Δt_u) is ascribed to the thermo-optic effect due to ring heating by the perturbing pulse, when it is close enough to the beginning of a subsequent SP stage so as to perturb it (e.g., see Fig. 3(a4)). Such a perturbation is then conveyed by the SP dynamics to the subsequent test signal. We notice that, in some cases, the oscillation of the memory effect as a function of Δt_p presents an increasing frequency as the mean optical input power is decreased (see Fig. 4(a1)–(a3), corresponding to the 2-ring system with a laser frequency of 192.328 THz, and input power of 1.04, 0.89, and 0.75 mW, respectivley).

To better explain the correlation plots in Fig. 4(a), a visual example is shown in Fig. 4(b), where test signals, corresponding to the case of the correlation plot (a1), are displayed one after another in different colours. In this case, the SP phase shift produced by different Δt_p values is cyclic, thus generating the periodic memory effect shown in Fig. 3(b). To visualize this cyclic behavior, the numbered arrows in Fig. 4(a1) and (b) indicate the specific SP stages where the correlation is close to one, i.e., the shape of the test signal is visually comparable to that of the sixth SP stage chosen as the reference (highlighted by the dotted line rectangle in (b)). Conversely, at points where the correlation is low, such as SP stage 34, the shape of the test signal is significantly different from that indicated by the arrows. As expected, this memory effect is enabled by the periodicity of the SP pattern and its consistent reproducibility across the different rectangular pulses that drive it. However, the long-term memory effect is not always periodic. For example, in the 3-ring system, with laser frequency of 192.44 THz and mean input power of 5.05 mW (see Fig. 4(c)), the reference test signal (highlighted by the dotted line rectangle) is not repeated again. This means that the corresponding Δt_p value produces a unique SP phase shift in the considered Δt_p range. Therefore, in principle, one could unambiguously detect that specific Δt_p value by simply looking at the test signal, with potential application to distributed acoustic sensing[27], where the timing of a pulse exiting the fibre sensor corresponds to a perturbation at a specific spatial point.

Spike rate detection

The results shown in the previous section (namely the oscillating memory effect as a function of Δt_p) suggest that some of the observed SP dynamics might be particularly sensitive to the rate of repeated perturbing pulses. Therefore, in this section we investigate how the change in SP dynamics due to sequences of perturbing pulses can be exploited to detect different perturbation rates. In the context of SNNs, such an effect can be seen as the capacity of the MRRs (considered as spiking neurons) to activate when excited by a certain spike rate.

We considered an input signal similar to the one described in the previous section, but with 20 SP stages (20 μs long each, with middle power) alternated with 10 μs long pauses (with low power, used to reset the SP between different stages), as shown in Fig. 5(a). Moreover, instead of a single perturbing pulse at different Δt_p values, we employed a sequence of 20 short pulses (50 ns duration each) starting at the same time but with different pulse rates (Fig. 5(a1) and (a2)). In particular, in the first SP stage, consecutive perturbing pulses are separated by 20 ns, corresponding to a high spiking rate of 1 spike every 70 ns. In the following 19 SP stages, the time separation of perturbing pulses gradually increases by 10 ns at a time, reaching 210 ns in the last SP stage.

Here we discuss three interesting responses of the 3-ring SCISSOR. First of all, we obtained a constant output power, which monotonically decreases with the perturbing spike rate (at laser frequency 192.433 THz and mean power of 0.93 mW, see Fig. 5(b)). This is emphasized in the zoomed-in area indicated by the yellow rectangle in Fig. 5(b1). Specifically, the red dashed horizontal line highlights that, as the rate of the spiking perturbation

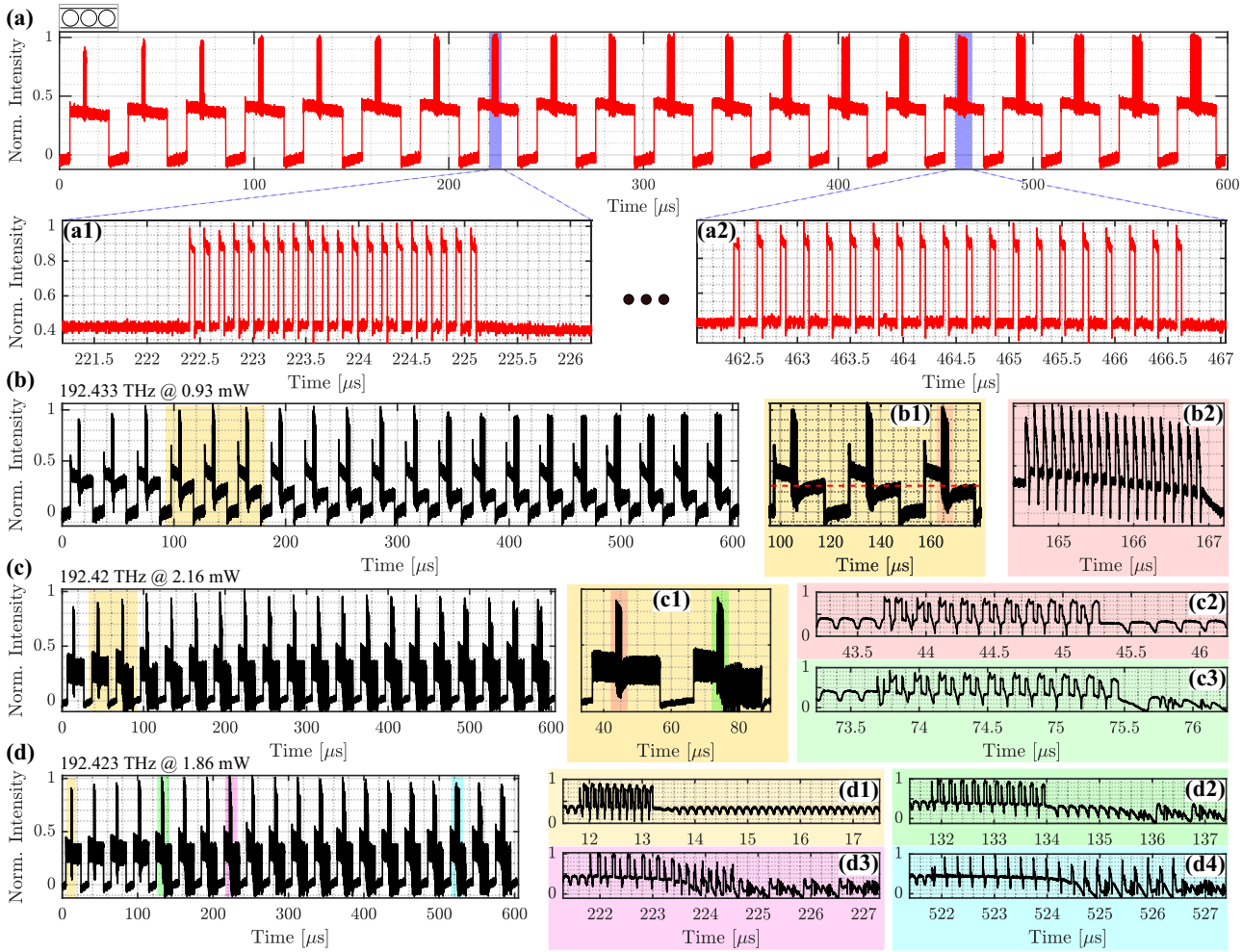

Fig. 5 | Spike rate detection using the 3-ring SCISSOR. a Input optical signal comprising 20 SP stages (long square pulses), each perturbed by 20 spikes with gradually increasing spike rates. **(a1)** and **(a2)** Zoomed-in views showing two perturbing spike sequences with different spike rate. **b** SCISSOR response at the reported laser frequency and power, showing that increasing spike rates produce responses with decreasing constant power level. **c**, **d** Varying the input frequency and power, we observe the existence of a spike rate threshold after which the SCISSOR response shows completely different SP dynamics. Note that the colored (**(b1) and (b2)**, **(c1)**–**(c3)**, and **(d1)**–**(d4)**) are zoom-in views of the corresponding colored areas in the adjacent left plots.

decreases, the outgoing field intensity reaches a constant lower value. In principle, such a response can be used to infer the pulse rate of the perturbation by just measuring the average output, e.g., with a slow photodetector and without a fast oscilloscope. Therefore, our system could be employed in smart sensing applications where fast dynamics are differentiated with cheaper components, without the need to measure fast signals. Panel (b2) shows the zoom of Fig. 5(b1) in the pink area, i.e., in the presence of the perturbation. Note that at this specific frequency and power, the 3-ring SCISSOR operates in a stable regime both before and after the perturbation, exhibiting a steady-state response without SP (no spikes).

The 3-ring SCISSOR can also detect spike rates that are lower than a certain threshold by permanently modifying its SP dynamics. In particular, at input frequency 192.42 THz and input power of 2.16 mW, we find that the SCISSOR's pulsing response is changed in shape, pulse frequency, and average output power by input spike rates larger than 1 spike every 80 ns (Fig. 5(c)). The zoom indicated by the yellow rectangle in Fig. 5(c1) shows an example of the response as the spike perturbation rate decreases. As shown in the additional zooms in red (panel (c2)) and green (panel (c3)), the time evolution before the spike rate perturbation presents the same SP behavior. In contrast, after the perturbation, the output response varies not only in the average power, but also in the frequency and pattern of the spikes. In fact, the different coloured panels show largely different lineshapes. Thus, this 3-rings system can be seen as a small spiking neural network which presents an activation function in the spiking rate dimension. It should be stressed that similar responses were obtained at different laser frequencies and input power, with varying spiking rate thresholds. Therefore, the spiking rate activation threshold can be arbitrarily chosen by modifying the constant optical input sustaining the SP dynamics.

Finally, our photonic circuit can also present significantly different SP dynamics as a result of being excited with different spiking rates (e.g., at a laser frequency of 192.423 THz and input power of 1.86 mW, see Fig. 5(d)). As seen in the zoomed-in areas indicated by the rectangles (highlighted in figure by yellow (panel (d1)), green (panel (d2)), pink (panel (d3)) and light blue (panel (d4)), the output SCISSOR response changes following the perturbation, resulting in spiking rate-dependent regimes. Note that even in this case, the early stages of SP, specifically before the spike perturbation, exhibit the same pattern. This shows that only three coupled MRRs can host very rich dynamics and display complex responses to periodic excitations. Such responses can be sustained over much longer time intervals w.r.t. the characteristic time scales of the underpinning nonlinear effects.

Conclusion

We experimentally studied the SP dynamics of coupled silicon MRRs (up to 3 rings) varying input wavelength and power. We demonstrated the potential of these compact structures as energy efficient building blocks for photonic SNNs and also for photonic sensing of high-speed optical signals, in the sub-μs time

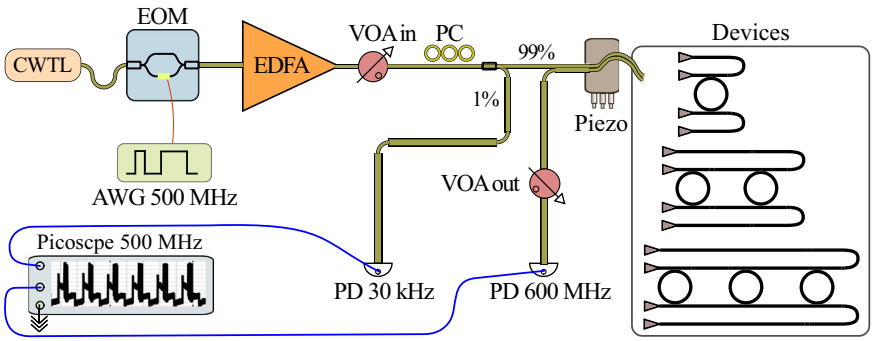

Fig. 6 | Schematic diagram of the experimental setup. The modulated light is coupled to the devices under test (single microresonator, 2-ring and 3-ring SCISSOR) by means of fibre array and grating couplers. The response of the device is detected by a photodetector and recorded on an oscilloscope. CWTL Continuous-wave tunable laser, EOM Electro-Optical Modulator, AWG Arbitrary Waveform Generator, EDFA Erbium Doped Amplifier, VOA Variable Optical Attenuator, PC Polarization Control and PD Photodetector. Sketches of the investigated structures are shown as devices: a microresonator in add-drop configuration and two SCISSORs consisting of two and three microresonators.

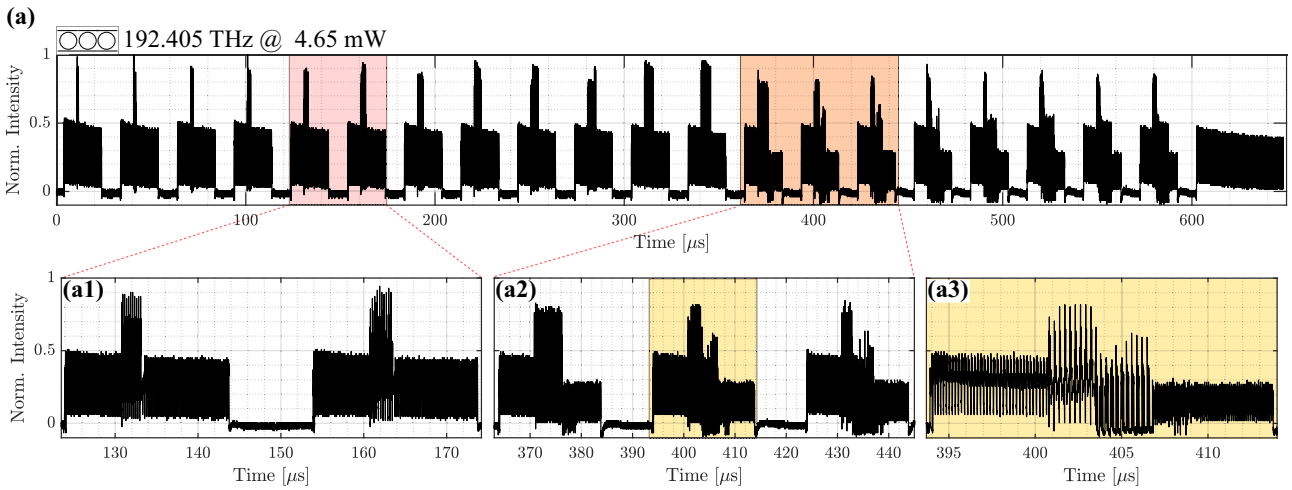

Fig. 7 | Spike rate detection. Response of the 3-ring SCISSOR to the same optical input lineshape of Fig. 5 (a) but with a larger input laser power and different input laser frequency as given in the plot. **a** Shows the full response, while **(a1)**–**(a3)** reports zoomed views at different time intervals. Note that the pink and orange boxes in (a) are enlarged in (a1) and (a2), respectively. While the yellow box in the panel in (a2) is enlarged in the (a3). A significant change in the SP frequency occurs at higher spiking rates and, therefore, at a lower perturbation average power. This change is not correlated with the duration of the perturbation, as it occurs before the perturbation ends. This can be observed in the yellow panel (a2).

scale. In particular, we showed that the spike rate of the pulsed responses can be tuned over a range spanning from around 2 to 20 μs. Several different response shapes could be achieved, where enhanced richness and complexity are obtained by increasing the number of coupled resonators.

Moreover, we demonstrated that SP dynamics can be exploited to extend the memory of MRRs by at least one order of magnitude, thus enabling their use in neuromorphic computing tasks with a much broader range of timescales. Furthermore, coupled MRRs displayed unique responses to certain perturbing pulse timings, which opens up opportunities for spike timing-dependent processing in neuromorphic photonics and for event detection applications.

Finally, we showed that our 3-ring structure can produce different long-lasting responses depending on the perturbation spike rate at its input. Such a response can be a constant output power proportional to the input spike rate, or even a complex pulsed signal whose shape abruptly changes once we overcome a certain input spike rate. This threshold depends on the wavelength and power of the constant input which causes the SP. Such a behaviour can be seen as an activation function in the spike rate dimension, which can be leveraged to build silicon photonics all-optical SNNs. Furthermore, the translation of sub-μs dynamics into a long-lasting effect is particularly interesting for high-speed sensing applications, as expensive and power-hungry high-speed electronics could be substituted.

Our results corroborate the potential for SP microresonators to be employed as building blocks of energy efficient and compact SNNs. Furthermore, we showed how the SP dynamics in these devices can be exploited to achieve all-optical long-term memory and pulse rate detection in an integrated photonic circuit, thus setting the groundwork for a new smart sensing framework based on time dependent optical signals. An exciting next step for this research is the combination of larger arrays of SP microresonators with machine learning to tackle complex sensing and detection tasks.

Methods

Samples

The devices under test are a MRR in add-drop configuration and two SCISSORs consisting of two and three coupled MRRs, respectively. A sketch of their top view is shown in Fig. 6, under "Devices". The MRRs are based on silicon waveguides (indicated by the black lines) with a cross-section of 450 nm × 220 nm embedded in a silica cladding. The MRRs have a ring shape with a radius of $r = 7\,\mu$m and are point-like coupled to two bus waveguides with gaps of 180 nm. In SCISSORs, the distance between the centres of MRRs is $3\pi r$. The input and output of the light signal are provided by grating couplers (≃3.5 dB coupling losses), shown in the Fig. 6 with gray triangles. The analysed structures were fabricated in different runs at the IMEC/Europractice facility within a multi-project wafer programme.

Experimental setup

The optical properties of single and coupled silicon MRRs are measured using the optical setup shown schematically in Fig. 6. A fiber-coupled Continuous-Wave Tunable Laser (Pure Photonics) operating at the C-band

is coupled to an Electro-Optic Modulator (EOM, iXblue model MXAN-LN-10) driven by an Arbitrary Waveform Generator (AWG, Teledyne model T3AFG500). The amplitude-modulated optical signal is amplified by an EDFA (Thorlabs) and attenuated to the desired power by an electronic Variable Optical Attenuator (VOA in). The resulting signal is adjusted in polarization by a Polarization Control (PC). A 1% tap is placed at the output of the PC to monitor the average input optical power using a slow Photo-Detector (PD 30 kHz, M2033). The remaining 99% of the signal is injected as input into the device to be analysed through a fibre array placed on a three-axis linear piezoelectric stage to ensure proper alignment. The fiber array collects the device output response which, after passing through a second electronic variable optical attenuator (VOA out), is measured by a fast photodetector (PD 600 MHz, Menlosystem model FPD610-FC-NIR). The electrical signals from the two PDs are read by an oscilloscope (Picoscope model 6000) and stored in a computer that controls the instruments of the setup. Note that the optical chip is mounted on a thermostat holder whose temperature is controlled by a proportional-integral-derivative controller connected to a Peltier cell and a 10 kΩ thermistor.

Further insights on spike rate detection

In section "Spike rate detection", we showed that a 3-ring SCISSOR can detect perturbations at certain spike rates. In this subsection, we explore this further by analyzing how changes in the SP dynamics correspond to different input perturbation rates. Our goal is to show that the coupled MRRs detect distinct spike rates, rather than just the length of the spike sequence or its average power.

Figure 7(a) shows a typical response of the 3-ring SCISSOR to 20 SP stages (see Fig. 5(a)), with the input laser set to a frequency of 192.405 THz and an average power of 4.65 mW. Figure 7(a1)–(a3) shows three enlarged views of this response. After the 20 SP stages, there is a longer SP stage, which is not perturbed and, therefore, it is used as a reference. During the full length of this reference SP stage, the SP dynamics remain stable. From this observation, we infer that no switch of SP dynamics occur spontaneously, i. e., without a perturbation.

The first 12 SP stages show no major changes in response after perturbation, although they are associated with higher spike rates, thus conveying higher average power. Indeed, as seen in the zoom of the fifth and sixth SP stages (Fig. 7(a1)), the SP signal remains largely unchanged after perturbation. However, SP dynamics switch at higher spike rates (as seen in the panel (a2)), corresponding to lower average power. This shift in dynamics cannot be attributed to the longer duration of the perturbation, since the panel (a3) shows a switching of SP dynamics occurring during the pulse train, before its end. Therefore, we conclude that the observed change in SP dynamics is caused by the spike rate of the perturbation rather than by its duration or average power.

Data availability

The data supporting the results of this study are available from the corresponding author upon reasonable request.

Code availability

The main Python code used to elaborate and analyze the raw data regarding the results shown in sections "Long-term memory enabled by self-pulsing" and "Spike rate detection", can be found at https://doi.org/10.5281/zenodo.13880494.

Received: 2 August 2024; Accepted: 11 November 2024;
Published online: 22 November 2024

References

1. Shastri, B. J. et al. Photonics for artificial intelligence and neuromorphic computing. *Nat. Photonics* **15**, 102–114 (2021).
2. Pavanello, F. et al. Special session: neuromorphic hardware design and reliability from traditional cmos to emerging technologies. In *2023 IEEE 41st VLSI Test Symposium (VTS)*, 1–10 (IEEE, 2023).
3. Xu, M. et al. Reconfigurable neuromorphic computing: materials, devices and integration. *Adv. Mater.* **35**, 2301063 (2023).
4. Christensen, D. V. et al. 2022 roadmap on neuromorphic computing and engineering. *Neuromorphic Comput. Eng.* **2**, 022501 (2022).
5. Covi, E. et al. Adaptive extreme edge computing for wearable devices. *Front. Neurosci.* **15**, 611300 (2021).
6. Lobo, J. L., Del Ser, J., Bifet, A. & Kasabov, N. Spiking neural networks and online learning: an overview and perspectives. *Neural Netw.* **121**, 88–100 (2020).
7. Nunes, J. D., Carvalho, M., Carneiro, D. & Cardoso, J. S. Spiking neural networks: a survey. *IEEE Access* **10**, 60738–60764 (2022).
8. Leuthold, J., Koos, C. & Freude, W. Nonlinear silicon photonics. *Nat. Photonics* **4**, 535–544 (2010).
9. Borghi, M., Castellan, C., Signorini, S., Trenti, A. & Pavesi, L. Nonlinear silicon photonics. *J. Opt.* **19**, 093002 (2017).
10. Johnson, T. J., Borselli, M. & Painter, O. Self-induced optical modulation of the transmission through a high-q silicon microdisk resonator. *Opt. Express* **14**, 817–831 (2006).
11. Biasi, S., Franchi, R., Bazzanella, D. & Pavesi, L. On the effect of the thermal cross-talk in a photonic feed-forward neural network based on silicon microresonators. *Front. Phys.* **10**, 1093191 (2022).
12. Van Vaerenbergh, T., Fiers, M., Dambre, J. & Bienstman, P. Simplified description of self-pulsation and excitability by thermal and free-carrier effects in semiconductor microcavities. *Phys. Rev. A* **86**, 063808 (2012).
13. Borghi, M., Bazzanella, D., Mancinelli, M. & Pavesi, L. On the modeling of thermal and free carrier nonlinearities in silicon-on-insulator microring resonators. *Opt. Express* **29**, 4363–4377 (2021).
14. Priem, G. et al. Optical bistability and pulsating behaviour in silicon-on-insulator ring resonator structures. *Opt. Express* **13**, 9623–9628 (2005).
15. Pavesi, L. Thirty years in silicon photonics: a personal view. *Front. Phys.* 709 (2021).
16. Mancinelli, M., Borghi, M., Ramiro-Manzano, F., Fedeli, J. & Pavesi, L. Chaotic dynamics in coupled resonator sequences. *Opt. Express* **22**, 14505–14516 (2014).
17. Van Vaerenbergh, T. et al. Cascadable excitability in microrings. *Opt. Express* **20**, 20292–20308 (2012).
18. Xiang, J., Torchy, A., Guo, X. & Su, Y. All-optical spiking neuron based on passive microresonator. *J. Lightwave Technol.* **38**, 4019–4029 (2020).
19. Xiang, J., Zhang, Y., Zhao, Y., Guo, X. & Su, Y. All-optical silicon microring spiking neuron. *Photonics Res.* **10**, 939–946 (2022).
20. Lugnan, A., Carrillo, S. G.-C., Wright, C. D. & Bienstman, P. Rigorous dynamic model of a silicon ring resonator with phase change material for a neuromorphic node. *Opt. Express* **30**, 25177–25194 (2022).
21. Zhang, Q. et al. On-chip spiking neural networks based on add-drop ring microresonators and electrically reconfigurable phase-change material photonic switches. *Photonics Res.* **12**, 755–766 (2024).
22. Biasi, S. et al. Photonic neural networks based on integrated silicon microresonators. *Intell. Comput.* **3**, 0067 (2024).
23. Biasi, S., Franchi, R., Cerini, L. & Pavesi, L. An array of microresonators as a photonic extreme learning machine. *APL Photonics* **8**, 096105 (2023).
24. Lugnan, A. et al. Emergent self-adaptation in an integrated photonic neural network for backpropagation-free learning. Preprint at *arXiv*. arXiv:2312.03802 (2023).
25. Bazzanella, D., Mancinelli, M., Borghi, M., Bettotti, P. & Pavesi, L. Precise photonic hybrid electromagnetic solver. *IEEE Photonics J.* **14**, 1–10 (2022).
26. Borghi, M., Biasi, S. & Pavesi, L. Reservoir computing based on a silicon microring and time multiplexing for binary and analog operations. *Sci. Rep.* **11**, 15642 (2021).
27. Muanenda, Y. et al. Recent advances in distributed acoustic sensing based on phase-sensitive optical time domain reflectometry. *J. Sens.* **2018**, 3897873 (2018).

Acknowledgements
We gratefully thank Dr. Giovanni Donati and Dr. Riccardo Franchi for useful suggestions and interesting discussions. This project has received funding from the European Research Council (ERC) under the European Union's Horizon 2020 research and innovation programme (grant agreement No. 788793, BACKUP), from the MIUR under the PRIN PELM project (20177 PSCKT) nad by the European Union under NextGenerationEU project PRIN2022AEEKNC. S. Biasi acknowledges the cofinancing of the European Union FSE-REACT-EU, PON Research and Innovation 2014-2020 DM1062/2021. A. Lugnan acknowledges funding by the European Union under GA n°101064322-ARIADNE. Views and opinions expressed are however those of the author(s) only and do not necessarily reflect those of the European Union or The European Research Executive Agency. Neither the European Union nor the granting authority can be held responsible for them.

Author contributions
S.B. and A.L. conceived the experiment. A.L performed the experimental measurements. S.B. and D.M. performed the first measurements to study the phenomenon of induced memory by self-pulsation. S.B. analyzed the self-pulsing response traces and created the figures, while A.L. focused on analyzing the memory traces and spike rate detection. A.L and S.B. wrote the manuscript. L.P supervised the work. All authors contributed to the revision of the manuscript.

Competing interests
The authors declare no competing interests.

Additional information
Supplementary information The online version contains supplementary material available at https://doi.org/10.1038/s42005-024-01869-2.

Correspondence and requests for materials should be addressed to Stefano Biasi.

Peer review information *Communications Physics* thanks Kathy Lüdge and the other, anonymous, reviewer(s) for their contribution to the peer review of this work.